

# Spin, charge and orbital ordering in ferrimagnetic insulator YBaMn<sub>2</sub>O<sub>5</sub>

R. Vidya\*, P. Ravindran, A. Kjekshus and H. Fjellvåg

*Department of Chemistry, University of Oslo, Box 1033, Blindern, N-0315 Oslo, Norway.*

(October 27, 2018)

## Abstract

The oxygen-deficient (double) perovskite YBaMn<sub>2</sub>O<sub>5</sub>, containing corner-linked MnO<sub>5</sub> square pyramids, is found to exhibit ferrimagnetic ordering in its ground state. In the present work we report generalized-gradient-corrected, relativistic first-principles full-potential density-functional calculations performed on YBaMn<sub>2</sub>O<sub>5</sub> in the nonmagnetic, ferromagnetic and ferrimagnetic states. The charge, orbital and spin orderings are explained with site-, angular momentum- and orbital-projected density of states, charge-density plots, electronic structure and total energy studies. YBaMn<sub>2</sub>O<sub>5</sub> is found to stabilize in a G-type ferrimagnetic state in accordance with experimental results. The experimentally observed insulating behavior appears only when we include ferrimagnetic ordering in our calculation. We observed significant optical anisotropy in this material originating from the combined effect of ferrimagnetic ordering and crystal field splitting. In order to gain knowledge about the presence of different valence states for Mn in YBaMn<sub>2</sub>O<sub>5</sub> we have calculated *K*-edge x-ray absorption near-edge spectra for the Mn and O atoms. The presence of the different valence states for Mn is clearly established from the x-ray absorption near-edge spectra, hyperfine field parameters and the magnetic properties study. Among the experimentally proposed structures, the recently reported description based on *P4/nmm* is found to represent the stable structure.

## I. INTRODUCTION

Perovskite-type transition-metal oxides  $ABO_3$  and their oxygen-deficient relatives exhibit a variety of interesting physical properties including high-temperature superconductivity, metal-insulator transition and a variety of cooperative magnetic phenomena. Among them manganites have recently attracted particular attention because of the discovery of colossal negative magnetoresistance (CMR) in  $La_{1-x}Sr_xMnO_3$ ,<sup>1</sup>  $La_{1-x}Ba_xMnO_3$ <sup>1</sup> and related phases.<sup>2-5</sup> This renewed interest in the mixed-valence manganese perovskites such as  $La_{1-x}Pb_xMnO_3$  is due to their potential technological applications.<sup>6,7</sup> In addition, the search for new high-temperature superconductors in mixed-oxide materials is a driving force for attention. The mechanism of high-temperature superconductivity is believed to be linked to cooperative interaction between copper  $3d_{x^2-y^2}$  and  $3d_{z^2}$  orbitals and oxygen  $2p$  orbitals.<sup>8</sup>

An attractive approach to obtain insight in the nature of this phenomenon is to examine the magnetic and electrical properties of non-copper oxide analogues of known high-temperature superconducting cuprates. Manganese is a good choice for such a task, as in an octahedral perovskite-like configuration,  $\text{Mn}^{3+}$  ( $d^4$  high spin with a single electron in an  $e_g$  orbital) will experience a similar Jahn-Teller (JT) distortion to that of  $\text{Cu}^{2+}$  [ $d^9$  high spin with three electrons (or one hole) in the  $e_g$  orbitals]. The hole-doped manganese perovskites show some similarities to the corresponding hole-doped Cu phases in which superconductivity occurs.<sup>9</sup> Structural similarities between these two groups of materials suggest that new Mn analogues of the high-temperature superconducting Cu oxides may be prepared.

Since the discovery of CMR phenomena in perovskite-related manganites, extensive studies have been performed on manganese oxides with atomic arrangements related to the perovskite and pyrochlore structures over a wide variety of compositions with the aim to explore exotic spin-charge coupled state.<sup>10</sup> Anisotropic CMR phenomena have also recently been reported in layered Ruddlesden-Popper variants of perovskites  $(RE, AE)_{n+1}\text{Mn}_n\text{O}_{3n+1}$  ( $RE$  = rare earth;  $AE$  = alkaline earth)<sup>11</sup> for  $n = 2$ . Similar effects have also been observed in the oxygen-deficient cubic pyrochlore  $\text{Tl}_2\text{Mn}_2\text{O}_{7-\delta}$ . The chemical features common to these materials are an intimately connected Mn-O-Mn network, within a three-dimensional or multi-layered structure, and an average Mn oxidation state between +3 and +4 (obtained by hole-doping of  $\text{Mn}^{3+}$ ).<sup>12</sup>

At low temperatures, manganese perovskites are characterized by strong competition between charge-carrier itineracy and localization. In the former case a ferromagnetic (F) metallic state is formed. In the latter case, the localized carriers tend to form charge-ordered (CO) states, which have a predominantly antiferromagnetic (AF) insulating character. Hence, we have a competition between F with metallic behavior and cooperative JT distortion with CO. The CO state can be converted into a F metallic state, by the application of a magnetic field. The intriguing doping-induced, temperature-dependent metal-insulator transition and the interwoven magnetic (spin), orbital and charge-ordering phenomena in mixed-valence manganese perovskites and transition-metal oxides have attracted much attention in recent years.<sup>13</sup> An active role of the orbital degree of freedom in the lattice and electronic response can be most typically seen in manganese perovskite oxides. As a matter of fact such properties appear to have their origin in the unique electronic structures derived from the hybridized Mn  $3d$  and O  $2p$  orbitals in the particular structural and chemical environment of a perovskite. The thus resulting intra-atomic exchange and the orbital degrees of freedom of the Mn  $3d$  electrons play essential roles in this constellation. Furthermore, various kinds of structural distortion profoundly influence the electronic properties. The extensive study of CMR in  $RE_{1-x}AE_x\text{MnO}_3$  have brought forth novel features related to CO in these oxides. In transition-metal oxides with their anisotropic-shaped  $d$  orbitals, Coulomb interaction between the electrons (strong electron correlation effect) may be of great importance. Orbital ordering (OO) gives rise to anisotropic interactions in the electron-transfer process which in turn favors or disfavors the double-exchange and the superexchange (F or AF) interactions in an orbital direction-dependent manner and hence gives a complex spin-orbital-coupled state. OO in the manganese oxides occasionally accompanies the concomitant CO.<sup>14</sup> The ordered oxygen-deficient double perovskites  $RE\text{BaT}_2\text{O}_{5+\delta}$  ( $T$  = transition metals like Fe, Co and Mn) have attracted much attention as new spin-charge-orbital coupled systems and new CMR materials. In the isostructural phases with  $RE = \text{Gd}$  and  $\text{Eu}$  CMR effects of

some 40% are observed.<sup>15</sup> As the experimental findings have been made available only in recent years, little theoretical work has been undertaken to understand the origin of these microscopic properties. The present study reports a detailed theoretical investigation on the electronic structure and optical properties of  $\text{YBaMn}_2\text{O}_5$ .

At low temperature,  $\text{YBaMn}_2\text{O}_5$  is an AF insulator with CO of  $\text{Mn}^{3+}$  and  $\text{Mn}^{2+}$  accompanied by OO and spin ordering (SO).<sup>25</sup> The mechanism of CO and SO in manganites is not at all clear. Different authors have emphasized the importance of different ingredients such as on-site Coulomb interactions,<sup>16–18</sup> JT distortion<sup>19,20</sup> and inter-site Coulomb interactions.<sup>21</sup> Therefore, we have attempted to study CO, OO and SO through full potential linear muffin-tin orbital (FPLMTO) and full potential linear augmented plane wave (FPLAPW) methods. Similar to  $\text{Fe}_3\text{O}_4$  and  $\text{SmBaFe}_2\text{O}_{5+w}$  where Fe takes the conventional valence states of  $\text{Fe}^{3+}$  and  $\text{Fe}^{2+}$  at low temperature,<sup>22,23</sup> Mn is reported to occur as  $\text{Mn}^{3+}$  and  $\text{Mn}^{2+}$  in  $\text{YBaMn}_2\text{O}_5$ . Above the so called Verwey temperature ( $T_V$ ) valence-state mixing has been observed in  $\text{Fe}_3\text{O}_4$  as well as in  $\text{SmBaFe}_2\text{O}_{5+w}$ . This brings in an additional interesting aspect in the study of the electronic structure and magnetic properties of Mn in  $\text{YBaMn}_2\text{O}_5$ . The first structure determinations based on powder x-ray (300 K)<sup>12</sup> and neutron (100–300 K)<sup>24</sup> diffraction data found that  $\text{YBaMn}_2\text{O}_5$  crystallizes in space group  $P4/mmm$ , whereas a more recent powder neutron (2–300 K)<sup>25</sup> diffraction study (PND) found  $P4/nmm$ . So, a theoretical examination of the total energy for the two different structural alternatives is required.

The rest of the paper is arranged as follows: Sec. II gives crystal structure details for  $\text{YBaMn}_2\text{O}_5$ . The theoretical methods used for the calculations are described in Sec. III. The analysis of the band structure is given in Sec. IV A. Sec. IV B deals with the nature of the chemical bonding in  $\text{YBaMn}_2\text{O}_5$ , analyzed with the help of site-, angular momentum- and orbital-projected density of states (DOS). Sec. IV C discusses CO and OO in  $\text{YBaMn}_2\text{O}_5$  with the help of charge density plots. The results from calculations of optical spectra and x-ray absorption near edge (XANE) spectra are discussed in Sec. IV D and IV E respectively. Sec. IV F deals with hyperfine parameters. Finally the important conclusions are summarized in Sec. V.

## II. CRYSTAL STRUCTURE

Chapman *et al.*<sup>12</sup> synthesized rather impure  $\text{YBaMn}_2\text{O}_5$  and reported the crystal structure parameters according to space group  $P4/mmm$  [described as double or ordered, oxygen-deficient perovskite; closely related to  $\text{YBaCuFeO}_5$ ]. These findings were subsequently confirmed by McAllister and Attfield<sup>24</sup> who also established a model for the ferrimagnetic ordering of the magnetic moments of Mn in  $\text{YBaMn}_2\text{O}_5$  (still based on an impure sample). More recently Millange *et al.*<sup>25</sup> have succeeded in preparing phase-pure  $\text{YBaMn}_2\text{O}_5$  and these authors report crystal and magnetic structure parameters according to space group  $P4/nmm$ .

Within the  $P4/nmm$  description  $\text{YBaMn}_2\text{O}_5$  crystallizes with  $a = 5.5359$  and  $c = 7.6151$  Å; Y in 2(b), Ba in 2(a), Mn(1) in 2(c) with  $z = 0.2745$ , Mn(2) in 2(c) with  $z = 0.7457$ , O(1) in 8(j) with  $x = 0.4911$ ,  $y = 0.9911$  and  $z = 0.4911$  and O(2) in 2(c) with  $z = 0.0061$ . The lacking oxygens in the yttrium plane, compared with the perovskite-aristotype structure reduces the coordinate number of yttrium to 8, while barium retains the typical

twelve coordination of the perovskite structure. The Mn-O network consists of double layers of  $\text{MnO}_5$  square pyramids, corner shared in the  $ab$  plane and linked *via* their apices.

According to the  $P4/nmm$  description (Fig. 1) the two kinds of  $\text{MnO}_5$  pyramids are arranged in an ordered manner, each  $\text{Mn}^{2+}\text{O}_5$  pyramid being linked to five  $\text{Mn}^{3+}\text{O}_5$  pyramids. Owing to this charge ordering, each  $\text{Mn}^{2+}$  has four  $\text{Mn}^{3+}$  in-plane neighbors. Oxygen takes two crystallographically different sites. O(1) forms the base of the square pyramids, while O(2) is located at the apex of the pyramids. The interatomic Mn-O distances fall in four categories, being 1.908 and 2.086 Å for  $\text{Mn}^{3+}\text{-O}(1)$  and  $\text{Mn}^{2+}\text{-O}(1)$ , respectively, whereas O(2) is 2.081 and 1.961 Å away from  $\text{Mn}^{3+}$  and  $\text{Mn}^{2+}$ , respectively. (The  $P4/mmm$  description gave on the other hand, almost equal basal and apical Mn-O distances within all square-pyramids.<sup>12</sup>) The basal plane  $\text{Mn}^{3+}\text{-O}(1)\text{-Mn}^{2+}$  angle is  $157.8^\circ$  and the apical  $\text{Mn}^{3+}\text{-O}(2)\text{-Mn}^{2+}$  angle is  $180^\circ$ . The large variation in these angles play a key role in the magnetic properties.

### III. COMPUTATIONAL DETAILS

#### A. The FPLMTO computations

The present calculations have used the full-potential linear muffin-tin orbital (FPLMTO) method<sup>26</sup> where no shape approximation is assumed for the one-electron potential and charge density. The basis geometry consists of muffin-tin (MT) spheres centered around the atomic sites with an interstitial region in between. Inside the MT spheres the charge density and potential are expanded by means of spherical harmonic functions multiplied by a radial component. The interstitial basis function is a Bloch sum of linear combinations of Neumann or Henkel functions depending on the sign of the kinetic energy  $\kappa^2$  (corresponding to the basis functions in the interstitial region). Each Neumann or Henkel function is then augmented (replaced) by a numerical basis function inside the MT spheres, in the standard way of the linear MT orbital method.<sup>27</sup> Since a Bloch sum of atomic centered Henkel or Neumann functions has the periodicity of the underlying lattice it may be expanded in a Fourier series, as done here. The spherical-harmonic expansion of the charge density, potential and basis functions was performed up to  $\ell_{max} = 6$ . The basis included Y  $4p$ ,  $5s$ ,  $5p$  and  $4d$  states, Ba  $5p$ ,  $6s$ ,  $6p$ ,  $5d$  and  $4f$  states, Mn  $4s$ ,  $4p$  and  $3d$  states and O  $2s$ ,  $2p$  and  $3d$  states.

Furthermore, the calculations are all-electron as well as fully relativistic. The latter level is obtained by including the mass velocity and Darwin (and higher order) terms in the derivation of the radial functions (inside the MT spheres) whereas the spin-orbit coupling was included at the variational step using an  $(\ell, s)$  basis. Moreover, the present calculations made use of a so-called double basis, to ensure a well-converged wave function. This means that two Neumann or Henkel functions were applied, each attached to its own radial function with an  $(n, \ell)$  quantum number. The integrations over the Brillouin zone (BZ) in the ground state calculations were performed as a weighted sum, using the special point sampling,<sup>28</sup> with weights reflecting the symmetry of a given  $\mathbf{k}$  point. We also used a Gaussian smearing width of 20 mRy for each eigenvalue in the vicinity of the Fermi level to speed up the convergence. For the DOS and optical calculations, the tetrahedron integration was employed. The calculations were performed for the experimentally determined structural parameters (see Sec. II). For the exchange-correlation functional,  $E_{xc}(n)$ , we have used the

generalized gradient approximation (GGA) where the gradient of the electron density is taken into account using Perdew and Wang<sup>29</sup> implementation of GGA. 192  $\mathbf{k}$  points in the irreducible part of the primitive tetragonal BZ were used for the self-consistent ground state calculations and 352  $\mathbf{k}$  points for the optical calculations.

## B. The FPLAPW computations

For the XANES and orbital-projected DOS calculations we have applied the full-potential linearized-augmented plane wave (FPLAPW) method<sup>30</sup> in a scalar-relativistic version without spin-orbit coupling. The FPLAPW method divides space into an interstitial region (IR) and non-overlapping MT spheres centered at the atomic sites. In IR, the basis set consists of plane waves. Inside the MT spheres, the basis set is described by radial solutions of the one-particle Schrödinger equation (at fixed energies), and their energy derivatives multiplied by spherical harmonics. The charge densities and potentials in the atomic spheres were represented by spherical harmonics up to  $\ell = 6$ , whereas in the interstitial region these quantities were expanded in a Fourier series with 3334 stars of the reciprocal lattice vectors  $\mathbf{G}$ . The radial basis functions of each LAPW were calculated up to  $\ell = 10$  and the non-spherical potential contribution to the Hamiltonian matrix had an upper limit of  $\ell = 4$ . Atomic-sphere radii  $R_{MT}$  of 2.5, 2.8, 1.8 and 1.6 a.u. for Y, Ba, Mn and O, respectively, were used. Since the spin densities are well confined within a radius of about 1.5 a.u, the resulting magnetic moments do not depend appreciably with the chosen atomic-sphere radii. The initial basis set included  $5s$ ,  $5p$ ,  $4d$  valence and  $4s$ ,  $4p$  semicore functions for Y,  $6s$ ,  $6p$ ,  $6d$  valence and  $5s$ ,  $5p$  semicore functions for Ba,  $4s$ ,  $4p$ ,  $3d$  valence and  $3s$ ,  $3p$  semicore functions for Mn and  $2s$ ,  $2p$  and  $3d$  functions for O. These basis functions were supplemented with local orbitals<sup>31</sup> for additional flexibility to the representation of the semicore states and for generalization of relaxation of the linearization errors. Owing to the linearization errors DOS are reliable only to about 1 to 2 Ry above  $E_F$ . Therefore, after selfconsistency was achieved for this basis set we included higher energy local orbitals:  $5d$ - and  $4f$ -like function for Y,  $6d$ - and  $4f$ -like function for Ba,  $5s$ - and  $5p$ -like functions for Mn and  $3p$ -like functions for O. The BZ integration was done with a modified tetrahedron method<sup>32</sup> and we used 140  $\mathbf{k}$  points in the irreducible wedge of BZ. Exchange and correlation effects are treated within density-functional theory (DFT), using GGA.<sup>29</sup>

## C. Optical properties

Optical properties of matter can be described by means of the transverse dielectric function  $\epsilon(\mathbf{q}, \omega)$  where  $\mathbf{q}$  is the momentum transfer in the photon-electron interaction and  $\omega$  is the energy transfer. At lower energies one can set  $\mathbf{q} = \mathbf{0}$ , and arrive at the electric dipole approximation, which is assumed throughout this paper. The real and imaginary parts of  $\epsilon(\omega)$  are often referred to as  $\epsilon_1$  and  $\epsilon_2$ , respectively. We have calculated the dielectric function for frequencies well above those of the phonons and therefore we considered only electronic excitations. In condensed matter systems, there are two contributions to  $\epsilon(\omega)$ , *viz.* intra-band and inter-band transitions. The contribution from intra-band transitions is important only for metals. The inter-band transitions can further be split into direct and indirect

transitions. The latter involves scattering of phonons and are neglected here, and moreover these only make small contribution to  $\epsilon(\omega)$  in comparison to the direct transitions,<sup>33</sup> but have a temperature broadening effect. Also other effects, *e.g.*, excitons (which normally give rise to rather sharp peaks) affect the optical properties.

The direct inter-band contribution to the imaginary part of the dielectric function,  $\epsilon_2(\omega)$  is calculated by summing all possible transitions from occupied to unoccupied states, taking the appropriate transition-matrix element into account. The dielectric function is a tensor for which all components are needed for a complete description. However, we restrict our considerations to the diagonal matrix elements  $\epsilon^{\nu\nu}(\omega)$  with  $\nu = x, y$  or  $z$ . The inter-band contribution to the diagonal elements of  $\epsilon_2(\omega)$  is given by

$$\epsilon_2^{\nu\nu} = \frac{8\pi^2 e^2}{m^2 \omega^2} \times \sum_n^{unocc} \sum_{n'}^{occ} \int_{BZ} |P_{nn'}^\nu(k)|^2 f_{kn}(1 - f_{kn'}) \delta(E_n^k - E_{n'}^k - \hbar\omega) \times \frac{d^3k}{(2\pi)^3}, \quad (1)$$

where  $e$  is the electron charge,  $m$  its mass,  $f_{kn}$  the Fermi-Dirac distribution function,  $P_{nn'}^\nu$  the projection of the momentum matrix elements along the direction  $\nu$  of the electric field and  $E_n^k$  one electron energies. The evaluation of the matrix elements in Eq. (1) is done separately over the MT and interstitial regions. Further details about the evaluation of matrix elements are found in Ref. 34. The integration over BZ in Eq. (1) is performed using linear interpolation on a mesh of uniformly distributed points, *i.e.*, the tetrahedron method. The total  $\epsilon_2^{\nu\nu}$  was obtained from  $\epsilon_2^{\nu\nu}(IBZ)$ , *i.e.*  $\epsilon_2^{\nu\nu}$  was calculated only for the irreducible ( $I$ ) part of BZ using

$$\epsilon_2(\omega) = \frac{1}{N} \sum_{i=1}^N \sigma_i^T \epsilon_2(IBZ) \sigma_i, \quad (2)$$

where  $N$  is the number of symmetry operations and  $\sigma_i$  represents the symmetry operations; for shortness,  $\epsilon(\omega)$  is used instead of  $\epsilon^{\nu\nu}(\omega)$ . Lifetime broadening was simulated by convoluting the absorptive part of the dielectric function with a Lorentzian, whose full width at half maximum (FWHM) is equal to  $0.005(\hbar\omega)^2$  eV. The experimental resolution was simulated by broadening the final spectra with a Gaussian of constant FWHM equal to 0.01 eV.

After having evaluated Eq. (2) we calculated the inter-band contribution to the real part of the dielectric function  $\epsilon_1(\omega)$  from the Kramers-Kronig relation

$$\epsilon_1(\omega) = 1 + \frac{2}{\pi} P \int_0^\infty \frac{\epsilon_2(\omega') \omega' d\omega'}{\omega'^2 - \omega^2}. \quad (3)$$

In order to calculate  $\epsilon_1(\omega)$  one needs a good representation of  $\epsilon_2(\omega)$  up to high energies. In the present work we have calculated  $\epsilon_2(\omega)$  up to 41 eV above the  $E_F$  level, which also was the truncation energy used in Eq. (3).

To compare our theoretical results with the experimental spectra we have calculated polarized reflectivity spectra using the following relation. The specular reflectivity can be obtained from the complex dielectric constant in Eq. (1) through the Fresnel's equation,

$$R^{\nu\nu}(\omega) = \left| \frac{\sqrt{\epsilon(\omega)} - 1}{\sqrt{\epsilon(\omega)} + 1} \right|^2. \quad (4)$$

We have also calculated the absorption coefficient  $I(\omega)$  and the refractive index  $n$  using the following expressions:

$$I(\omega) = 2\omega \left( \frac{(\epsilon_1^2(\omega) + \epsilon_2^2(\omega))^{1/2} - \epsilon_1(\omega)}{2} \right)^{1/2} \quad (5)$$

and

$$n = \left( \frac{\sqrt{\epsilon_1^2 + \epsilon_2^2} + \epsilon_1}{2} \right)^{1/2}. \quad (6)$$

## IV. RESULTS AND DISCUSSION

### A. Electronic band structure

The FPLMTO calculations were performed on  $\text{YBaMn}_2\text{O}_5$  for three different magnetic configurations, *viz.*, paramagnetic (P), ferromagnetic (F) and antiferromagnetic (AF). From Table I it can be seen that in the AF configuration, the spins are not cancelled and hence this state is really ferrimagnetic (Ferri). Moreover, Table I shows that Ferri  $\text{YBaMn}_2\text{O}_5$  has lower energy than the P and F configurations. The energy-band structure of Ferri  $\text{YBaMn}_2\text{O}_5$  is shown in Fig. 2a and 2b for up- and down-spin bands, respectively.  $\text{YBaMn}_2\text{O}_5$  is seen to be an indirect-band-gap semiconductor. A closer inspection of the energy-band structure shows that the band gap is between the top of the valence band (VB) at the  $\Gamma$  point and the bottom of the conduction band (CB) at the  $Z$  point. As the unit cell contains 18 atoms, the band structure is quite complicated and Fig. 2 therefore only depicts energy range of  $-7.5$  to  $7.5$  eV.

There is a finite energy gap of 1.307 eV between the top-most occupied VB and the bottom-most unoccupied CB in the up-spin channel. For the purpose of more clarity, it is convenient to divide the occupied portion of the band structure in the up-spin channel into three energy regions: (i) Bands lying at and below  $-4$  eV. (ii) Bands lying between  $-4$  and  $-2$  eV. (iii) The top of VB, closer to  $E_F$ , *viz.*, the range  $-2$  to  $0$  eV. Region (i) contains 17 bands with contributions from Y  $4s$ ,  $5s$ , Mn  $3s$ ,  $3d$  and O  $2p$  electrons. Region (ii) comprises bands which originate from completely filled O(1) and O(2)  $2p$  orbitals. Region (iii) includes 10 bands. Among them one finds delocalized (dispersed) bands originating from Y  $5s$  and O  $2p$  orbitals and somewhat localized bands attributed to Mn(1)  $d_{z^2}$ ,  $d_{x^2-y^2}$ ,  $d_{xz}$  and  $d_{yz}$  orbitals. The top-most occupied band contains electrons stemming from the Mn  $d_{z^2}$  orbital. In the unoccupied portion of the band structure, a corresponding division leads to two energy regions: (1) The bottom-most CB from  $0$  to  $2$  eV and (2) the middle range of CB from  $2$  to  $4$  eV. (Above  $4$  eV the bands are highly dispersed and it is quite difficult to establish the origin of the bands.) There are 9 bands in region (1) which have some Y  $5s$ , Ba  $5d$ , Mn(1)  $3d_{xy}$  and Mn(2)  $3d$  characters. In region (2) the bands retain Y  $6s$ ,  $4d$ , Ba  $7s$ ,  $5d$  and Mn  $4s$ ,  $4p$  and  $3d$  characters.

The energy band structure of the down-spin channel (Fig. 2b) has 16 bands in the region (i) up to  $-4$  eV which arise from the  $s$  and  $p$  electrons of the Y, Ba, Mn and O atoms. The

mainly  $s$  and  $p$  electron character of the bands, makes them appreciably dispersed. The second energy region (ii) contains 12 bands, which have Y  $5s$ , Ba  $5p$ , Mn(2)  $3d$  and O(1), O(2)  $2p$  character. The third region (iii) closer to  $E_F$  has 10 bands which are mainly arising from Mn(1), Mn(2)  $3d$  and O(1), O(2)  $2p$  orbitals. Unlike the up-spin channel the down-spin channel contains two bands at  $E_F$  which arise from the originally half-filled  $t_{2g}$  orbitals of Mn(1) and the half-filled  $d_{xy}$  orbital of Mn(2).

A finite band gap of 1.046 eV opens up between the highest occupied VB and bottom-most unoccupied CB. The unoccupied portion of the down-spin channel is quite different from that of the up-spin channel. The lowest-lying unoccupied band has Mn(2)  $4s$  electrons. Between 0 and 2 eV there are 8 bands which arise mainly from Mn(1)  $3d$  electrons as well as from Mn(1), Mn(2)  $4s$  electrons and O(1), O(2)  $2p$  electrons. The dispersed bands present between 2 and 4 eV have Y  $5s$ ,  $3d$ , Ba  $6s$ ,  $5d$  and Mn(1)  $3d$  characters.

## B. DOS characteristics

In order to theoretically verify which of the two ( $P4/mmm$  or  $P4/nmm$  based) structures is energetically more stable, we performed first-principle calculations for both variants. The calculated DOS value at  $E_F$  for the P phase  $P4/mmm$  variant is 192.82 states/(Ry f.u.) and for  $P4/nmm$  149 states/(Ry f.u.) in the P state. Hence, a larger number of electrons are present at  $E_F$  for the former variant, which favours the relative structural stability of the latter. Moreover, our calculations show that the  $P4/nmm$  variant is 860 meV/f.u. lower in energy than the  $P4/mmm$  variant. Therefore we conclude that YBaMn<sub>2</sub>O<sub>5</sub> is more stable in space group  $P4/nmm$  than in  $P4/mmm$ , *viz.* in accordance with the most recent PND-based experimental study.

Our calculated total DOS curves for YBaMn<sub>2</sub>O<sub>5</sub> in the P, F and Ferri configurations are given in Fig. 3. The highest occupied energy level in VB, *i.e.*,  $E_F$  is marked by the dotted line. In the P and F cases finite DOS values are present in the vicinity of  $E_F$ . Hence, both the P and F configurations exhibit metallic character. On going from the P to F case, the electrons start to localize which is seen from the reduced number of states at  $E_F$ . Due to the electron localization, the gain in total energy of 3.1 eV (Table I) is observed when the spin-polarization is include in our calculations. However, in the Ferri case, a finite band gap of 0.88 eV opens up between the top of VB and the bottom of CB. The experimental studies also show semiconducting behavior.<sup>12,35</sup> From Table I it can be seen that the Ferri configuration has lower energy than the other two configurations. The present observation of the stabilization of a Ferri ground state in YBaMn<sub>2</sub>O<sub>5</sub> is consistent with the established magnetic structure.<sup>25</sup> It is interesting to note that the introduction of the Ferri configuration is essential in order to obtain the correct semiconducting ground state for YBaMn<sub>2</sub>O<sub>5</sub>. Unlike LaMnO<sub>3</sub> (where the energy difference between the F and AF cases is  $\sim 25$  meV)<sup>36</sup> there is large energy difference ( $\sim 0.5$  eV) between the Ferri and the F states of YBaMn<sub>2</sub>O<sub>5</sub>. So, a very large magnetic field is required to stabilize the F phase and induce insulator-to-metal transition in YBaMn<sub>2</sub>O<sub>5</sub>.

In the REMnO<sub>3</sub> phases hole doping induces CE-type magnetic ordering in which the spins are F aligned in zigzag chains with AF coupling between these chains. In YBaMn<sub>2</sub>O<sub>5</sub>, the Mn spins are AF aligned within quasi-one-dimensional chains as well as between the chains. The main difference between YBaMn<sub>2</sub>O<sub>5</sub> and REMnO<sub>3</sub> is that the latter have  $e_g$

electrons present in the vicinity of  $E_F$  and that the superexchange interaction originates from the localized  $t_{2g}$  electrons. Owing to the square-pyramidal crystal field in  $\text{YBaMn}_2\text{O}_5$  the  $e_g$  electrons also get localized and hence both  $e_g$  and the  $t_{2g}$  electrons participate in the superexchange interaction. This is the main reason why the F state has much higher energy than the AF state in  $\text{YBaMn}_2\text{O}_5$  as compared with  $\text{LaMnO}_3$ .

To obtain more insight into the DOS features, we show the angular momentum- and site-decomposed DOS in Fig. 4. The lower panels for Y and Ba show that, in spite of the high atomic numbers for Y and Ba, small DOS values are seen in VB. The Y and Ba states come high up in CB (*ca.* 4 eV above  $E_F$ ) indicating a nearly total ionization of these atoms. They lose their valence charge to form ionic bonding with oxygen. According to the crystal structure, Y and Ba are located in layers along  $c$ , which is clearly reflected in the electronic charge-density distribution within (110) in the AF configuration (Fig. 6).

The distinction between Mn(1) and Mn(2) is clearly reflected in the different topology of their DOS curves. As seen from Table I, Mn(1) has a smaller magnetic moment ( $3.07 \mu_B$ ) than Mn(2) ( $3.91 \mu_B$ ) which leads to the conclusion that Mn(1) corresponds to  $\text{Mn}^{3+}$  and Mn(2) to  $\text{Mn}^{2+}$ , both in high-spin states. Both Mn(1) and Mn(2) have low-lying DOS features around  $-17$  eV which can be attributed to well-localized  $s$  and  $p$  electrons originating from the covalent interaction between Mn  $3d$  with O  $2s$  and  $2p$  states. The somewhat dispersed DOS in the energy region  $-7.5$  to  $-2.5$  eV is attributed to  $3d$  electrons for both Mn(1) and Mn(2). As Mn(1) and Mn(2) are AF coupled, their  $d$ -orbital DOS have opposite character. The localized peaks closer to  $E_F$ , with a width of about 2 eV, have both ( $3d$ )  $e_g$  and  $t_{2g}$  character (see below).

The top two panels of Fig. 4 show DOS for O(1) and O(2). Crystallographically O(1) is co-planar (in  $ab$ ) with Mn, whereas O(2) is at the apex of the square pyramid (along  $c$ ). The well-localized peaks in DOS for O(1) and O(2) at about  $-18$  eV reflect the completely filled  $2s$  orbitals. The spread-out DOS features between  $-7.5$  to  $-0.5$  eV are attributed to O  $2p$  states. Fig. 4 shows that the O  $2p$  states are energetically degenerate with Mn  $3d$  states in this energy range, implying that these orbitals form covalent bonds with Mn(1) and Mn(2) through hybridization. The almost empty DOS for O(1) and O(2) in CB implies that the oxygen atoms are in nearly completely ionized states in  $\text{YBaMn}_2\text{O}_5$ .

In order to progress further in the understanding of the chemical bonding, charge, spin and orbital ordering in  $\text{YBaMn}_2\text{O}_5$ , we have plotted the orbital-decomposed DOS for the  $3d$ -orbitals of Mn(1) and Mn(2) in Fig. 5. This illustration shows that DOS for the  $d_{z^2}$  orbital for both Mn(1) and Mn(2) are well-localized. There is a sharp peak at  $-5$  eV in the up-spin panel for Mn(1) and in the down-spin panel for Mn(2) which correlates with a well-localized peak in DOS for O(2) (Fig. 4) This is attributed to the  $180^\circ$  Mn $^{3+}$ -O(2)-Mn $^{2+}$  bond angle which facilitates  $p$ - $d$   $\sigma$  bond to the O(2)  $p_z$  orbital and superexchange interaction.<sup>37</sup> As up-spin Mn(1) and down-spin Mn(2) are involved, we infer that the superexchange interaction results in AF spin ordering between the Mn atoms involved. The peaks at *ca.* 1 eV in up-spin Mn(1) and down-spin Mn(2) are attributed to the (non-bonding)  $d_{z^2}$  orbitals.

Turning to the other  $e_g$  orbitals (of  $d_{x^2-y^2}$  character) for Mn(1) and Mn(2), these are spread in the  $ab$  plane. From Fig. 4, we see that the O  $2p$  orbitals are also situated in the same energy range ( $-5$  eV to 0) as the  $d_{x^2-y^2}$  orbitals of Mn(1) and Mn(2), thus these orbitals and O  $p_x$  and  $p_y$  orbitals form  $p$ - $d$   $\sigma$  bond. As the bond angle Mn(1)-O(1)-Mn(2) is only  $157^\circ$ , the strength of this covalent bond is weak and consequently the AF superexchange

interaction becomes weakened.<sup>37</sup> Despite the AF superexchange interaction, there is no exact cancellation of the spins of Mn(1)<sup>3+</sup> and Mn(2)<sup>2+</sup>, and the result is a Ferri state with a finite magnetic moment of 0.85  $\mu_B$ .

Transition-metal perovskite oxides which exhibit CO like La<sub>1-x</sub>Sr<sub>x</sub>MnO<sub>3</sub> have an octahedral crystal field, whereas YBaMn<sub>2</sub>O<sub>5</sub> has a square-pyramidal arrangement around Mn. In this case the  $d$  orbitals of Mn split into low-lying  $e_g$  orbitals and relatively higher-lying  $t_{2g}$  orbitals. Fig. 5, shows that  $t_{2g}$  is closer to  $E_F$  than  $e_g$ . The same feature is observed for the isostructural phase YBaCo<sub>2</sub>O<sub>5</sub>.<sup>38</sup> From crystal-structure considerations it is deduced that HOMO (highest occupied molecular orbital) is located at the top of the bonding  $\pi$  level of VB, arising from the Mn  $t_{2g}$  orbitals with a band gap to the empty LUMO (lowest unoccupied molecular orbital) located at the bottom of the antibonding  $\pi^*$  level of CB.<sup>35</sup> Among the  $t_{2g}$  orbitals  $d_{xz}$  and  $d_{yz}$  of both Mn(1) and Mn(2) are energetically degenerate as clearly seen from the character of the DOS curve. (In YVO<sub>3</sub> also  $d_{xz}$  and  $d_{yz}$  are nearly degenerate<sup>39</sup>.) So Mn(1) and Mn(2) exist in high-spin state with the  $e_g$  orbitals filled up before the  $t_{2g}$  orbitals. The  $d_{xz}$  and  $d_{yz}$  orbitals contain one electron each for Mn(1) and Mn(2). For Mn(1) a very small peak is seen, which could come from down-spin  $d_{xy}$ , whereas a finite sized peak is observed for the same orbital of Mn(2). It is indeed the occupancy of this orbital which determines the magnetic moment of Mn(1) and Mn(2). If one considers the Goodenough-Kanamori<sup>40</sup> rules for magnetic interactions in manganese oxides, the expected magnetic order should be A-type AF (*viz.* F ordering within the layers and AF ordering between the layers; arising from superexchange interactions between occupied  $d_{x^2-y^2}$  orbitals on Mn<sup>2+</sup> and empty  $d_{x^2-y^2}$  on Mn<sup>3+</sup>). However, owing to the large deviation of the Mn-O-Mn bond angle from 180° along with CO the  $d_{x^2-y^2}$  orbitals for both Mn species become occupied. Hence, AF ordering is observed between Mn within the planes as well as between the planes (see Fig. 7). One Mn couples AF to its six neighboring Mn in a G-type AF arrangement in accordance with experimental findings.<sup>25</sup> Hence, the theoretical calculations have provided the correct ground state with respect to the experiments.

Magnetic susceptibility and magnetization measurements, have unequivocally shown that YBaMn<sub>2</sub>O<sub>5</sub> is in a Ferri state at low temperature<sup>12,25</sup> with a saturated moment between 0.5 and 0.95  $\mu_B$  per YBaMn<sub>2</sub>O<sub>5</sub> formula unit.<sup>12,25</sup> The theoretically calculated magnetic moments for Mn are 3.07 and 3.93  $\mu_B$ , respectively, giving a net magnetic moment of 0.86  $\mu_B$  per formula unit for the Ferri state of YBaMn<sub>2</sub>O<sub>5</sub>. Our theoretically calculated value is less than the predicted (spin-only) value of 1.0  $\mu_B$ . From the DOS analyses, we noted that there is strong hybridization between Mn 3d electrons and O 2p electrons. A finite magnetic moment of 0.0064 and 0.0032  $\mu_B$ /atom are theoretically found to be present at O(1) and O(2), respectively. Hence, we conclude that the slight deviation in the saturated magnetic moment from that predicted by an idealized ionic model can be attributed to the strong hybridization between Mn 3d and O 2p electrons. We have also performed calculations with the room temperature structural parameters, confirming that the two manganese atoms possess different magnetic moments at this temperature.

### C. Charge and orbital ordering

For the pseudo-cubic and layered perovskite manganese oxides, essentially three parameters control the electron-correlation strength and the resultant structural, transport and

magnetic properties.<sup>10</sup> First, the hole-doping level (charge-carrier density or the band-filling level of CB). In the case of perovskite oxides the substitution of trivalent  $RE$  by divalent  $AE$  introduces holes in the Mn  $3d$  orbitals. Second, the effective one-electron bandwidth ( $W$ ) or equivalently the  $e_g$  electron-transfer interaction. The magnitude of  $W$  is directly determined by the size of the atom at the  $RE$ ,  $AE$  site which makes the Mn-O-Mn bond angle deviate from  $180^\circ$  and thus hinders the electron-transfer interaction. The correlation between CO and the size of  $RE$  and  $AE$  is studied by several workers and is well illustrated by a phase diagram in Ref. 41. Third comes the dimensionality: the lowering of the electronic dimensionality causes a variety of essential changes in the electronic properties. The carrier-to-lattice coupling is so strong in manganites, that the charge-localization tendency becomes very strong. In general the ground state of mixed-valent manganite perovskites is, therefore, either F and metallic or AF and CO. In all CO systems, the magnetic susceptibility drops rapidly at the CO temperature ( $T_{CO}$ ). CO drastically influences the magnetic correlations in manganites. Investigations on the CO state have established an intimate connection to lattice distortion. It seems to be the lattice distortion associated with OO which localizes the charge and thus initiates CO.<sup>41</sup> The effect of the CO state on cooperative magnetic states is to produce insulating behavior. A high magnetic field induces a melting-like phenomenon of the electron lattice of the CO phase giving rise to a huge negative magnetoresistance.<sup>42</sup> For these reasons, it is interesting to study CO in  $YBaMn_2O_5$ .

Charge localization, which is a prerequisite for CO is mutually exclusive with an F state according to and the double-exchange mechanism. The double-exchange mechanism requires hopping of charge carriers from one Mn to an adjacent Mn via an intervening O. The CO state is expected to become stable when the repulsive Coulomb interaction between carriers dominates over the kinetic energy of the carriers. Hence, CO arises because the carriers are localized at specific long-range-ordered sites below the CO temperature. CO is expected to be favored for equal proportions of  $Mn^{2+}$  and  $Mn^{3+}$  as in the present case, and in  $YBaMn_2O_5$  it is associated with the AF coupling between Mn in the  $ab$  plane. CO does not occur in  $Pr_{0.5}Sr_{0.5}MnO_3$ <sup>10</sup> where A-type AF is the ground state, whereas CO is observed in  $Nd_{0.5}Sr_{0.5}MnO_3$ <sup>10</sup> below 150 K where CE-type AF is the ground state. CO depends on the  $d$ -electron bandwidth and hence it is worth to consider this feature in some detail. On reduction of the Mn-O-Mn angle, the hopping between the Mn  $3d$  and O  $2p$  orbital decreases and hence the  $e_g$  bandwidth decreases. Consequently the system stabilizes in a Ferri-CO-insulating state. Usually the CO-insulating state transforms to a metallic F state on the application of a magnetic field. This may be the reason for the metallic behavior of the F phase found in our calculation. CO in  $YBaMn_2O_5$  is characterized by the real-space ordering of  $Mn^{2+}$  and  $Mn^{3+}$  species. Our calculations predict that a long-range CO of  $Mn^{2+}$  and  $Mn^{3+}$  with a rocksalt-type arrangement occurs at low temperatures. This can be viewed as chains of  $Mn^{2+}$  and  $Mn^{3+}$  running parallel to  $b$  and correspondingly alternating chains running along  $a$  and  $c$  (*viz.* a checker-board arrangement as seen from Fig. 7).

Furthermore, there exists orbital degrees of freedom for the  $e_g$  electrons and OO can lower the electronic energy through the JT mechanism. Therefore, mixed-valent manganites can have OO in addition to CO.<sup>43</sup> OO gives rise to the anisotropy in the electron-transfer interaction. This favors or disfavors the double-exchange interaction and the (F or AF) superexchange interaction in an orbital-dependent manner and hence gives a complex spin-orbital-coupled state. Therefore, it is also interesting to study OO in some detail. Fig. 6

shows the electron charge density of  $\text{YBaMn}_2\text{O}_5$  in (001) and (110) planes. The electron-charge density is plotted in the energy range where the  $3d$  orbitals reside, the shape of the  $d_{x^2-y^2}$  and  $d_{z^2}$  orbitals are well reproduced in Fig. 6a and b, respectively. In Fig. 6a, Mn(1), O(1) and Mn(2) are linked through covalent bonds which is easily seen as the finite electron density on the connecting lines between the atoms. This illuminates the path for the AF superexchange interaction between them. When the size of  $RE$  and  $AE$  becomes smaller the one-electron bandwidth (or  $e_g$  electron-transfer interaction) decreases in value.<sup>41</sup> For  $\text{Y}^{3+}$  with an ionic radius of  $1.25 \text{ \AA}$ , [smaller than other  $RE$ s like  $\text{La}^{3+}$  ( $1.36 \text{ \AA}$ )<sup>39</sup>] the Mn(1)-O(1)-Mn(2) angle is much less than  $180^\circ$  so the  $e_g$  electron bandwidth is small compared with the  $t_{2g}$  electron bandwidth. Fig. 6a shows that despite the finite electron density between Mn and O, the  $p$  orbitals of O are not directed towards the lobes of the Mn  $d_{x^2-y^2}$  orbitals. Hence, the strength of the resulting  $p$ - $d$  covalent bond is decreased. The orbital projected DOS in Fig. 5 shows that the  $t_{2g}$  bandwidth is larger than the  $e_g$  bandwidth owing to this hybridization effect.

The transfer integral between the two neighboring Mn atoms in the crystal lattice is determined by the overlap between the  $3d$  orbitals with the  $2p$  orbital of O atom. Fig. 6b shows the electron density along (110) of the unit cell. The  $d_{z^2}$  orbital is ordered along  $c$  and for both Mn(1) and Mn(2), this orbital hybridizes with the O(1)  $p_z$  orbital resulting in a  $p$ - $d$   $\pi$  bond. However, as the  $d_{z^2}$  orbital forms a strong  $\sigma$  bond with the  $p_z$  orbital of O(2), the strength of this  $\pi$  bond is weak. The overlap between the  $d_{x^2-y^2}$  and  $p_z$  orbitals is zero because of their different orientation in the  $ab$  plane. Therefore, the electron in the  $d_{x^2-y^2}$  orbital can not hop along  $c$ .<sup>37</sup> In this manner the  $e_g$  electrons get localized and cause CO and OO. Owing to the fact that the Mn(1)-O(1) bond length is  $1.908 \text{ \AA}$  compared with  $2.086 \text{ \AA}$  for Mn(2)-O(1), more electronic charge is present on  $\text{Mn}^{2+}$  than on  $\text{Mn}^{3+}$ . This is visible in the orbital decomposed DOS (Fig. 5), where the  $d_{xy}$  orbital of  $\text{Mn}^{2+}$  has more states (electrons) than that of  $\text{Mn}^{3+}$ . In cubic perovskites, the electron transfer is almost prohibited along  $c$  because of the orbital ordering of  $d_{x^2-y^2}$ , which is also the origin of the inter-plane AF coupling.<sup>14</sup>

PND<sup>25</sup> indicates that  $\text{Mn}^{3+}$  has the occupied  $d_{z^2}$  orbital extending along  $[001]$ , whereas the unoccupied  $d_{x^2-y^2}$  orbital extends along  $[110]$  and  $[1\bar{1}0]$ . A corresponding OO could be expected for  $\text{Mn}^{2+}$  with both  $d_{z^2}$  and  $d_{x^2-y^2}$  orbitals occupied. However, our detailed electronic structure studies show that both  $d_{z^2}$  and  $d_{x^2-y^2}$  orbitals are partially occupied for  $\text{Mn}^{2+}$  as well as  $\text{Mn}^{3+}$  as shown in Fig. 5. On the other hand, according to our charge-density analysis (Fig. 6a and b) the  $d_{z^2}$  orbital is ordered along  $[001]$  and  $d_{x^2-y^2}$  along  $[110]$  for Mn(1) and Mn(2) (Fig. 7), which is consistent with experimental findings. The Mn(1)-O-Mn(2) bond angle is much smaller than  $180^\circ$  which reduces the effective  $e_g$ - $e_g$  hopping, the  $e_g$  bands get localized and the bandwidth reduced. This is the main reason for OO in  $\text{YBaMn}_2\text{O}_5$ . Both  $d_{z^2}$  and  $d_{x^2-y^2}$  orbitals are aligned in the same orientation within the layer as well as between the layers as shown in Fig. 7. So, this type of OO is named F type.

#### D. Optical properties

Further insight into the electronic structure can be obtained from the calculated inter-band optical functions. It has been earlier found that the calculated optical properties for  $\text{SnI}_2$ ,  $\text{NaNO}_2$  and  $\text{MnX}$  ( $X = \text{As}, \text{Sb}, \text{Bi}$ )<sup>45-47</sup> are in excellent agreement with the

experimental findings, and we have therefore used the same theory to predict the optical properties of  $\text{YBaMn}_2\text{O}_5$ . Since, this material possesses unique Ferri ordering and insulating behavior along with an uniaxial crystal structure it may find application in optical devices. Yet another reason for studying the optical properties is that, it has been experimentally established<sup>44</sup> that the optical anisotropy of  $\text{Pr}_{0.6}\text{Ca}_{0.4}\text{MnO}_3$  is drastically reduced above  $T_{\text{CO}}$ . It is therefore expected that the optical anisotropy will provide more insight about CO and OO in  $\text{YBaMn}_2\text{O}_5$ . For  $\text{YBaMn}_2\text{O}_5$  with its tetragonal crystal structure, the optical spectrum is conveniently resolved into two principal directions  $E||a$  and  $E||c$  *viz.* with the electric field vector polarized along  $a$  and  $c$ , respectively. In the top-most panel of Fig. 8, the dispersive part of the diagonal elements of the dielectric tensor are given. The anisotropy in the dielectric tensor is clearly seen in this illustration.

In the second panel of Fig. 8, the polarized  $\epsilon_2$  spectra are shown. The spectrum corresponding to  $E||a$  and  $E||c$  differ from one another up to *ca.* 10 eV whereas less difference is noticeable in the spectra above 10 eV. Since there is an one-to-one correspondance between the inter-band transitions and band structures (discussed in Sec. IV A), we investigate the origin of the peaks in the  $\epsilon_2$  spectrum with the help of our calculated band structure. As  $\text{YBaMn}_2\text{O}_5$  stabilizes in the Ferri state, VB has an unequal number of bands in the up- and down-spin channels (Fig. 2), *viz.* 36 bands in the former and 38 in the latter. The two extra bands of the down-spin channel closer to  $E_F$  in VB play an important role in the transitions as discussed below. We name the top-most band of VB as no. 38 and bottom-most band of CB as no. 39. The lowest-energy peak A results from inter-band transitions (no. 35 to 41, mostly O(1)  $2p$  to Mn(2)  $d_{z^2}$  and no. 35 to 39, mostly Mn(1)  $d_{z^2}$  to Mn(2)  $4p$ ) and peak B results from transitions (no. 38 to 48 and 36 to 49, mostly Mn  $3d$  to Mn  $4p$ ). The peak C originates from many transitions, including O  $2p$  to Mn  $3d$ , Y  $5s$  to Y  $5p$  *etc.* Peaks D, E and F are contributed by several transitions including O  $2p$  to Mn  $3d$ , Y  $5s$  to Y  $5p$ . Further, a very small peak is present in the higher-energy region ( $\sim 17$  eV) of  $\epsilon_2$  which is due to transitions from lower-lying occupied levels to higher-lying unoccupied levels. The accumulation of broad Y  $4d$  and Ba  $5d$  bands in the high-energy part of CB results in very little structure in the higher-energy part of the optical spectra. The optical gaps for  $E||a$  and  $E||c$  are approximately the same indicating that the effective inter-site Coulomb correlation is the same for the in-plane and the out-of-plane orientation for the Ferri phase. This can be traced back to the G-type Ferri coupling in this material.

In order to understand the origin of the optical anisotropy in  $\text{YBaMn}_2\text{O}_5$  we have also made optical property calculations for the F phase, which show that (in contrast to the Ferri phase) the  $\epsilon_2$  spectrum for  $E||a$  is shifted some 3.5 eV to higher values than  $E||c$ . Further, the  $\epsilon_2$  components of  $E||c$  for the F phase is much smaller than that for the Ferri phase indicating that the large optical anisotropy in  $\text{YBaMn}_2\text{O}_5$  is originating from the G-type Ferri ordering.

To emphasize the above finding, we have also plotted the spin-projected  $\epsilon_2$  spectra along the  $a$  [ $\epsilon_2^a(\omega)$ ] and  $c$  [ $\epsilon_2^c(\omega)$ ] directions (third and fourth panels of Fig. 8, respectively). Although the optical gap is approximately same for  $E||a$  and  $E||c$  in the  $\epsilon_2$  spectrum, there is a finite difference in the optical gaps related to up- and down-spin electrons in the  $\epsilon_2^a(\omega)$  and  $\epsilon_2^c(\omega)$  spectra. The optical gap for the down-spin case is smaller than that for up-spin case owing to the presence of the two narrow bands very close to  $E_F$  in the down-spin channel of VB. There is a large difference between the spectra for up- and down-spins up to *ca.*

7 eV. The  $\epsilon_2^a(\omega)$  spectrum resulting from the up-spin states has somewhat more dispersed peaks than that from down-spin states. The  $\epsilon_2^a(\omega)$  spectrum resulting from the down-spin states has four well-defined peaks; two prominent peaks in the region 1.75 to 2 eV, and two additional peaks at *ca.* 2.25 and 3 eV. The magnitude of the down-spin peaks are higher than those of the up-spin peaks in the  $\epsilon_2^a(\omega)$  spectrum. The  $\epsilon_2^c(\omega)$  spectrum originating from up- and down-spin states have appreciable differences up to *ca.* 6 eV. The down-spin part has two well-defined peaks at *ca.* 1.75 and 2.75 eV. The up-spin part has dispersed peaks of lower magnitude than the down-spin part, the magnitude of the up-spin peaks in  $\epsilon_2^c(\omega)$  being generally higher than in  $\epsilon_2^a(\omega)$ . The optical anisotropy is noticeable in the direction- as well as spin-resolved  $\epsilon_2$  spectra. Hence, it is verified that the optical anisotropy originates both from crystal field effects as well as from the Ferri ordering. As reflectivity, absorption coefficient and refractive index are often subjected to experimental studies, we have calculated these quantities and reproduced them in Fig.9. We now advertice for experimental optical studies on YBaMn<sub>2</sub>O<sub>5</sub>.

### E. XANES studies

X-ray absorption spectroscopy (XAS) has developed into a powerful tool for the elucidation of the geometric and electronic structure of amorphous and crystalline solids.<sup>48</sup> X-ray absorption occurs by the excitation of core electrons, which makes this technique element specific. Although the X-ray absorption near edge structure (XANES) only provides direct information about the unoccupied electronic states of a material, it gives indirect information about the valence of a given atom in its particular environment and about occupied electronic states. This is because the unoccupied states are affected by the occupied states through interaction with the neighbors.

The oxygen atoms are in two different chemical environment in YBaMn<sub>2</sub>O<sub>5</sub> as clearly seen in PDOS in Fig. 4. The calculated *K*-edge spectra for O(1) and O(2) shown in Fig. 10 involve transition from the 1*s* core state to the unoccupied *p* state. In this context the Mn *K*-edge mainly probes the unoccupied Mn 4*p* states. It is generally accepted that O *K*-edge spectra is very sensitive to the local structure of transition-metal oxides as documented for Fe<sub>2</sub>O<sub>3</sub><sup>49</sup> and TiO<sub>2</sub><sup>50</sup>. The *K*-edge spectra for O(1) and O(2) (Fig. 10) show appreciable differences throughout the whole energy range. In particular there are two peaks appearing in the O(2) spectrum between 540 and 550 eV that are absent for O(1). Within 3 Å, 2 Mn, 2 Y and 6 O surround O(1) whereas, 2 Mn, 4 Ba and 5 O surround O(2). It is this different chemical environment which causes the differences in the *K*-edge XANES spectra of O(1) and O(2).

YBaMn<sub>2</sub>O<sub>5</sub> contains Mn in the valence states Mn<sup>3+</sup> and Mn<sup>2+</sup> which as discussed in Sec. IV C, experience CO. An experimental technique to visualize CO is not available. In order to visualize the presence of different oxidation states for Mn, we have theoretically calculated the XANES *K*-edge spectra for these and presented them in Fig. 10. Both Mn atoms are seen to have four peaks within the energy range considered, reflecting that both are surrounded by five O within 2.08 Å. However, owing to the different valence states there are intensity differences as well as energy shifts (some 1 eV) of these peaks. For example, the lower-energy peak has large intensity in the Mn(2) *K*-edge spectrum compared with that for Mn(1). On the contrary, the three higher-energy peaks in the Mn(2) *K*-edge

spectrum are less intense than in the Mn(1)  $K$ -edge spectrum. When experimental XANES spectra become available for YBaMn<sub>2</sub>O<sub>5</sub> the above features should be able to confirm the two different valence states for Mn.

## F. Hyperfine parameters

The calculation of hyperfine parameters is useful to characterize different atomic sites in a given material. Many experimental techniques such as Mössbauer spectroscopy, nuclear magnetic and nuclear quadrupole resonance and perturbed angular correlation measurements are used to measure hyperfine parameters. Hyperfine parameters describe the interaction of a nucleus with electric and magnetic fields created by its chemical environment. The resulting splitting of nuclear energy levels is determined by the product of a nuclear and an extra-nuclear quantity. In the case of quadrupole interaction, it is the nuclear quadrupole moment that interacts with the electric-field gradient (EFG) produced by the charges outside the nucleus<sup>53</sup>. EFG is a ground state property of a material which depends sensitively on the asymmetry of the electronic charges. The direct relation of EFG and the asphericity of the electron density in the vicinity of the probe nucleus enables one to estimate the quadrupole splitting and the degree of covalency or ionicity of the chemical bonds provided the nuclear quadrupole moment is known. Quantities describing hyperfine interactions (*e.g.* EFG and isomer shift) are widely studied nowadays both experimentally and theoretically.

Blaha *et al.*<sup>54</sup> have showed that the linear augmented plane wave (LAPW) method is able to predict EFGs in solids with high precision. The charge distribution of complex materials such as YBa<sub>2</sub>Cu<sub>3</sub>O<sub>7</sub>, YBa<sub>2</sub>Cu<sub>3</sub>O<sub>6.5</sub> and YBa<sub>2</sub>Cu<sub>3</sub>O<sub>6</sub> have been studied theoretically by Schwarz *et al.*<sup>55</sup> by this approach. In this study, we have attempted to establish the different valence states of Mn in YBaMn<sub>2</sub>O<sub>5</sub> with the help of EFG and the hyperfine field calculated using FPLAPW method as embodied in the WIEN97 code.<sup>30</sup>

The total hyperfine field (HFF) can be decomposed in three terms: a dominant Fermi contact term, a dipolar term and an orbital contribution. We limit our consideration to the contact term, which in the non-relativistic limit is derived from the spin densities at the nuclear site:

$$H_c = \frac{8}{3}\pi\mu_B^2[\rho_\uparrow(0) - \rho_\downarrow(0)] \quad (7)$$

EFG is defined as the second derivative of the electrostatic potential at the nucleus, written as a traceless tensor. This tensor can be obtained from an integral over the non-spherical charge density  $\rho(r)$ . For instance the principal component  $V_{zz}$  is given by

$$V_{zz} = \int d^3r \rho(\mathbf{r}) \frac{2P_2(\cos\theta)}{r^3} \quad (8)$$

where  $P_2$  is the second-order Legendre polynomial. A more detailed description of the calculation of EFG can be found elsewhere.<sup>56</sup>

The calculated EFG and HFF at the atomic sites in YBaMn<sub>2</sub>O<sub>5</sub> are given in Table II which confirm that there is a finite difference in the value of both EFG and HFF between the two Mn atoms. So we can conclude that their charge distribution is quite different. The higher value of EFG and HFF in Mn<sup>2+</sup> than in Mn<sup>3+</sup> is justified because, more charge is

found on the former. This can be seen from the orbital projected DOS as well as from the magnetic moments possessed by the two ions. HFF for  $\text{Mn}^{3+}$  in  $\text{LaMnO}_3$  is found to be  $-198 \text{ kG}^{36}$  which is quite close to  $-179 \text{ kG}$  found for  $\text{Mn}^{3+}$  in our case. Consequently we substantiate that Mn(1) corresponds to  $\text{Mn}^{3+}$ . The two oxygen ions also differ mutually in their values for EFG and HFF (Table II) suggesting that the strength of the covalent bond formed by them with Mn(1) and Mn(2) is different.

## V. SUMMARY

Like hole-doped  $RE\text{MnO}_3$ -based CMR materials  $\text{YBaMn}_2\text{O}_5$  also carries mixed-valence states of manganese, ferrimagnetic ordering, charge ordering and apparently undergoes a combined insulator-to-metal and Ferrimagnetic-to-Ferromagnetic transition. Hence  $\text{YBaMn}_2\text{O}_5$  may be a potential CMR material which deserves more attention.

We have made a detailed investigation on the electronic properties of  $\text{YBaMn}_2\text{O}_5$  using the full potential LMTO method as well as the full potential LAPW method and conclude the following.

1. The G-type ferrimagnetic insulating state is found to be the ground state in accordance with experimental findings.

2. The existence of the two different types of Mn atoms is visualized by differences in site- and orbital- projected DOS curves. In order to further emphasize the different valence states of Mn, we have calculated  $K$ -edge XANE spectra. For Mn as well as O the existence of two types of valence induced atomic species is established with the help of  $K$ -edge spectra.

3. The occurrence of checker-board-type charge ordering and F-type orbital ordering is seen from the charge-density plots. The small size of  $\text{Y}^{3+}$  makes the Mn-O-Mn bond angle deviate from  $180^\circ$ , which in turn imposes a reduction in the  $e_g$  bandwidth. The charge- and orbital-ordering features are believed to result from this perturbation of the  $e_g$  orbitals.

4. As  $\text{YBaMn}_2\text{O}_5$  is an ferrimagnetic insulator, it is useful to probe its optical properties for potential applications. We have analyzed the inter-band contributions to the optical properties with the help of the calculated electronic-band-structure features. We found large anisotropies in the optical spectra originating from ferrimagnetic ordering and the crystal field splitting. No experimental optical study of  $\text{YBaMn}_2\text{O}_5$  is hitherto available.

5. Hyperfine parameters such as hyperfine field and electric-field gradients have also been calculated showing very large differences in the computed values for the crystallographically different manganese and oxygen atoms. This substantiates that Mn exist in two different valence states in  $\text{YBaMn}_2\text{O}_5$ .

## ACKNOWLEDGMENTS

This work has received support from The Research Council of Norway (Programme for Supercomputing) through a grant of computing time. RV wishes to thank Dr. John Wills and Prof. Karlheinz Schwarz for supplying their computer codes used in this study and Prof. Olle Eriksson for useful communications. RV kindly acknowledges Dr. Leif Veseth and P. Vajeeston for the useful discussions.

## REFERENCES

- \* Electronic address: ravindran.vidya@kjemi.uio.no
- <sup>1</sup> A. Fujimori, T. Mizokawa and T. Saitoh in *Colossal Magnetoresistance, Charge Ordering and Related Properties of Manganese Oxides*, edited by C.N.R.Rao and B.Reveau (World Scientific, Singapore, 1998), p. 279.
- <sup>2</sup> R. Mahendiran, A.K. Raychaudhuri, A. Chainani, D.D. Sarma and S.B. Ray, *Appl. Phys. Lett.* **66**, 233 (1995).
- <sup>3</sup> J.Z. Liu, I.C. Chang, S. Irons, P. Klavins, R.H. Shelton, K. Song and S.R. Wasserman, *Appl. Phys. Lett.* **66**, 3218 (1995).
- <sup>4</sup> G.Q. Gong, C. Canedy, G.Xiao, J.Z. Sun, A. Gupta and W.J. Gallagher, *Appl. Phys. Lett.* **67**, 1783 (1995).
- <sup>5</sup> V. Caignaert, A. Maignan and B. Raveau, *Solid State Commun.* **95**, 357 (1995).
- <sup>6</sup> N. Furukawa, *J. Phys. Soc. Jpn.* **63**, 3214 (1994); Y. Tokura, A. Urushibara, Y. Moritomo, T. Arima, A. Asamitsu, G. Kido and N. Furukawa, *J. Phys. Soc. Jpn.* **63**, 3931 (1994).
- <sup>7</sup> A.J. Millis, P.B. Littlewood and B.I. Shraiman, *Phys. Rev. Lett.* **74**, 5144 (1995).
- <sup>8</sup> M.A. Dixon, *Physica C* **174**, 117 (1991).
- <sup>9</sup> J.B. Torrance, A. Bezing, A.I. Nazzari, T.C. Huang, S.S. Parkin, D.T. Keane, S. L. La Placa, P. A. Horn and G.A. Held, *Phys. Rev. B.* **40**, 8872 (1989).
- <sup>10</sup> H. Kuwahara and Y. Tokura in *Colossal Magnetoresistance, Charge Ordering and Related Properties of Manganese Oxides*, edited by C.N.R.Rao and B.Reveau (World Scientific, Singapore, 1998), p. 217.
- <sup>11</sup> Y. Moritomo, A. Asamitsu, H. Kuwahara and Y. Tokura, *Nature* **380** 141, (1996).
- <sup>12</sup> J. P. Chapman, J. P. Attfield, M. Mölgg, C. M. Friend and T.M. Beales, *Angew. Chem. Int. Ed. Engl.* **35**, 2482 (1996).
- <sup>13</sup> T. Vogt, P.M. Woodward, P. Karen, B.A. Hunter, P. Hennig and A.R. Moodenbaugh, *Phys. Rev. Lett.* **84**, 2969 (2000).
- <sup>14</sup> Y. Tokura, N. Nagaosa, *Science* **288**, 462 (2000).
- <sup>15</sup> C. Martin, A. Maignan, D. Pelloquin, N. Nguyen and B. Raveau, *Appl. Phys. Lett.* **71**, 1421 (1997).
- <sup>16</sup> V.I. Anisimov, J.S. Eflimov, M.A. Korotin and K. Terakura, *Phys. Rev. B* **55**, 15494 (1997).
- <sup>17</sup> W. Koshibae, Y. Kawamura, S. Ishihara and S. Okamoto, *J. Phys. Soc. Jpn.* **66**, 957 (1997).
- <sup>18</sup> T. Mizokawa and A. Fujimori, *Phys. Rev. B* **56**, R493 (1997).
- <sup>19</sup> J. Lee, J. Yu and K. Terakura, *J. Korean Phys. Soc.* **33**, S55 (1998).
- <sup>20</sup> I. Solovyev, N. Hamada and K. Terakura, *Phys. Rev. Lett.* **76**, 4825 (1996).
- <sup>21</sup> J.D. Lee and B.I. Min, *Phys. Rev. B* **55**, R14713 (1997).
- <sup>22</sup> P.A. Cox, *Transition Metal Oxides* (Clarendon, Oxford, 1992); E.J.W. Verwey and P.W. Haayman, *Physica (Amsterdam)* **8**, 979 (1941).
- <sup>23</sup> J. Linden, P. Karen, A. Kjekshus, J. Miettinen, T. Pietari and M. Karppinen, *Phys. Rev. B*, **60**, 15251 (1999).
- <sup>24</sup> J.A. McAllister and J.P. Attfield, *Materials Science Forum* **278-281**, 744 (1998).
- <sup>25</sup> F. Millange, E.Suard, V. Caignaert and B. Raveau, *Mat. Res. Bull.* **34**, 1 (1999).
- <sup>26</sup> J.M. Wills (unpublished); J.M. Wills and B.R. Cooper, *Phys. Rev. B* **36**, 3809 (1987); D.L. Price and B.R. Cooper, *ibid* **39**, 4945 (1989).

- <sup>27</sup> O.K. Andersen, Phys. Rev. B **12**, 3060 (1975).
- <sup>28</sup> D.J. Chadi and M.L. Cohen, Phys. Rev. B **8**, 5747 (1973); S. Froyen, *ibid* **39**, 3168 (1989).
- <sup>29</sup> J.P. Perdew in *Electronic Structure of Solids*, edited by P. Ziesche and H. Eschrig (Akademie Verlag, Berlin, 1991), p. 11; J.P. Perdew, K. Burke and Y. Wang, Phys. Rev. B **54**, 16533 (1996); J.P. Perdew, S. Burke and M. Ernzerhof, Phys. Rev. Lett. **77**, 3865 (1996).
- <sup>30</sup> P. Blaha, K. Schwarz and J. Luitz, WIEN97, Vienna Univ. of Tech. 1997. [An improved and updated Unix version of the original copyrighted code published by P. Blaha, K. Schwarz, P.I. Sorantin and S.B. Trickey, Comput. Phys. Commun. **59**, 399 (1990)].
- <sup>31</sup> D. Singh, Phys. Rev. B **43**, 6388 (1991).
- <sup>32</sup> P. Blöchl, O. Jepsen and O.K. Andersen, Phys. Rev. B **49**, 16223, (1994).
- <sup>33</sup> N.V. Smith, Phys. Rev. B **3**, 1862 (1971).
- <sup>34</sup> M. Alouani and J.M. Wills, Phys. Rev. B **54**, 2480 (1996).
- <sup>35</sup> T.P. Beales, M. Mölgg, J. Jutson and C.M. Friend, Phys. stat. sol. (a), **161**, 271 (1997)
- <sup>36</sup> P. Ravindran, A. Kjekshus, H. Fjellvåg, A. Delin and O. Eriksson (unpublished).
- <sup>37</sup> J.B. Goodenough, *Magnetism and the Chemical Bond* (Wiley, NewYork, 1963).
- <sup>38</sup> S.K. Kwon, J.H. Park and B.I. Min, Phys. Rev. B **62**, 14637 (2000).
- <sup>39</sup> H. Sawada and K. Terakura, Phys. Rev. B **58**, 6831 (1998).
- <sup>40</sup> J.B. Goodenough, Phys. Rev. **100**, 564 (1955); J. Kanamori, J. Phys. Chem. Solids, **10**, 87 (1959).
- <sup>41</sup> C.N.R. Rao and A.K. Raychauduri in *Colossal Magnetoresistance, Charge Ordering and Related Properties of Manganese Oxides*, edited by C.N.R. Rao and B. Raveau (World Scientific, Singapore, 1998), p. 1.
- <sup>42</sup> Y. Tokura, H. Kuwahara, Y. Moritomo, Y. Tomioka and A. Asamitsu, Phys. Rev. Lett. **76**, 3184 (1996).
- <sup>43</sup> S.-W. Cheong in *Colossal Magnetoresistance, Charge Ordering and Related Properties of Manganese Oxides*, edited by C.N.R. Rao and B. Raveau (World Scientific, Singapore, 1998), p. 241.
- <sup>44</sup> Y. Okimoto, Y. Tomioka, Y. Onose, Y. Otsuka and Y. Tokura, Phys. Rev. B **57**, R9377, (1998).
- <sup>45</sup> P. Ravindran, A. Delin, R. Ahuja, B. Johansson, S. Auluck, J.M. Wills and O. Eriksson, Phys. Rev. B **56**, 6851 (1997).
- <sup>46</sup> P. Ravindran, A. Delin, O. Eriksson, B. Johansson and J.M. Wills, Phys. Rev. B **59**, 1776 (1999).
- <sup>47</sup> P. Ravindran, A. Delin, B. Johansson, J.M. Wills and O. Eriksson, Phys. Rev. B **59**, 15680 (1999).
- <sup>48</sup> P. Behrens, Trends Anal. Chem. **11**, 218 (1992).
- <sup>49</sup> J.H. Paterson and O.L. Krivanek, Ultramicroscopy **32**, 313 (1990).
- <sup>50</sup> V.S. Lusvardi, M.A. Barteau, J.G. Chen, J. Eng. Jr. and A.V. Teplyakov, Surf. Sci. **397**, 237 (1998)
- <sup>51</sup> J.G. Chen, C.M. Kim, B. Frühberger, B.D. DeVries and M.S. Touvelle, Surf. Sci. **321**, 145 (1994).
- <sup>52</sup> J.G. Chen, B. Frühberger and M.L. Colaianni, J. Vac. Sci. Technol. A **14**, 1668 (1996).
- <sup>53</sup> H.M. Petrelli, P.E. Blöchl, P. Blaha and K. Schwarz, Phys. Rev. B **57**, 14690 (1998).
- <sup>54</sup> P. Blaha, K. Schwarz and P. Herzig, Phys. Rev. Lett. **54**, 1192 (1985).

<sup>55</sup> K. Schwarz, C. Ambrosch-Draxl and P. Blaha, Phys. Rev. B **42**, 2051 (1990).

<sup>56</sup> P. Blaha, K. Schwarz and P.H. Dederichs, Phys. Rev. B **37**, 2792 (1988); K. Schwarz, C. Ambrosch Draxl and P. Blaha, Phys. Rev. B **44**, 5141 (1991); K. Schwarz and P. Blaha, Z. Naturforsch. **47a**, 197 (1992).

TABLES

TABLE I. Total energy in different magnetic configurations

Type	Paramagnetic	Ferromagnetic	Antiferromagnetic
Total energy (Ry/f.u.)	-28438.0466	-28438.2754	-28438.3125
$\Delta E$ (meV/f.u.)	3618.6	505.6	0.0
Electronic state	Metal	Metal	Insulator
Calculated Magnetic Moment ( $\mu_B$ )			
Magn. mom.	Ferromagnetic	Antiferromagnetic	Experimental <sup>25</sup>
Mn <sup>3+</sup>	3.45	3.07	2.91
Mn <sup>2+</sup>	3.99	3.93	3.91
Saturated	7.44	0.86	0.95

TABLE II. Calculated (FLAPW method) principal component of the electric field gradient (EFG)  $V_{zz}$  in units of  $10^{21}$  V/m<sup>2</sup> and the Fermi contact hyperfine field (HFF) in kG at the atomic sites in ferro- and ferrimagnetic configurations.

Atom	Ferromagnetic		Ferrimagnetic	
	EFG	HFF	EFG	HFF
Y	0.17	45.90	0.48	21.01
Ba	10.50	-19.24	10.08	38.85
Mn(1)	2.41	-73.36	0.09	-179.54
Mn(2)	-0.98	-210.98	1.01	318.79
O(1)	5.36	64.42	4.95	-42.59
O(2)	3.86	97.06	5.06	21.96

## FIGURES

FIG. 1. The  $\text{YBaMn}_2\text{O}_5$  crystal structure. The Y and Ba ions form layers along  $c$ . The square pyramids corresponding to  $\text{Mn}^{3+}$  and  $\text{Mn}^{2+}$  are shown by open and shaded polyhedra, respectively. The O atoms at the bases and apices of the square pyramids are denoted O(1) and O(2), respectively.

FIG. 2. The electronic band structure of  $\text{YBaMn}_2\text{O}_5$  in the antiferromagnetic state; (a) up-spin bands and (b) down-spin bands. The line at 0 eV refers to the Fermi energy level.

FIG. 3. Total density of states (DOS) for  $\text{YBaMn}_2\text{O}_5$  in para-, ferro- and ferrimagnetic states.

FIG. 4. Site and angular momentum decomposed DOS of  $\text{YBaMn}_2\text{O}_5$  in the ferrimagnetic state, obtained by the full-potential LMTO method.

FIG. 5. Orbital ( $d$ ) decomposed DOS for Mn(1) and Mn(2) in the ferrimagnetic state obtained by the full-potential FLAPW method.

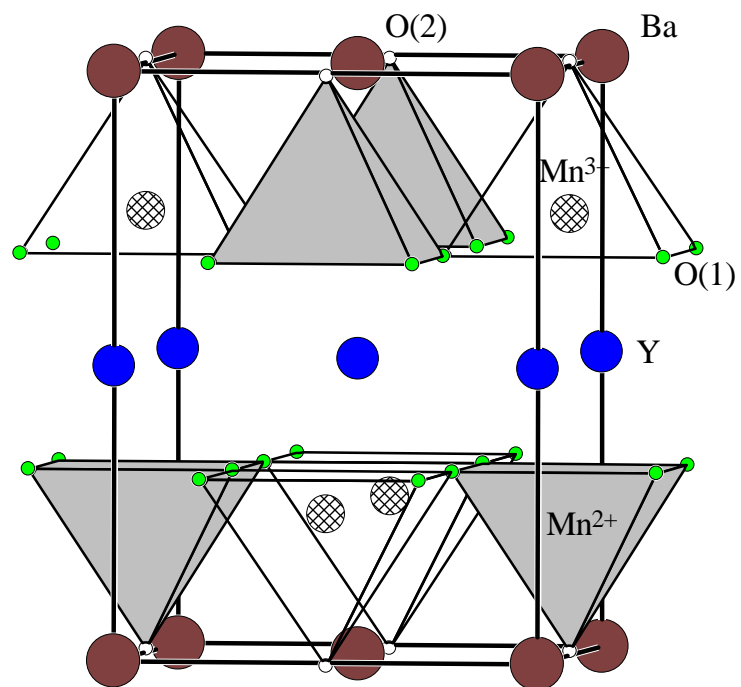
FIG. 6. Valence-charge distribution of  $\text{YBaMn}_2\text{O}_5$  in (a) (001) and (b) (110) plane. 75 contours are drawn between 0.01 and 0.1 electrons/a.u.<sup>3</sup>

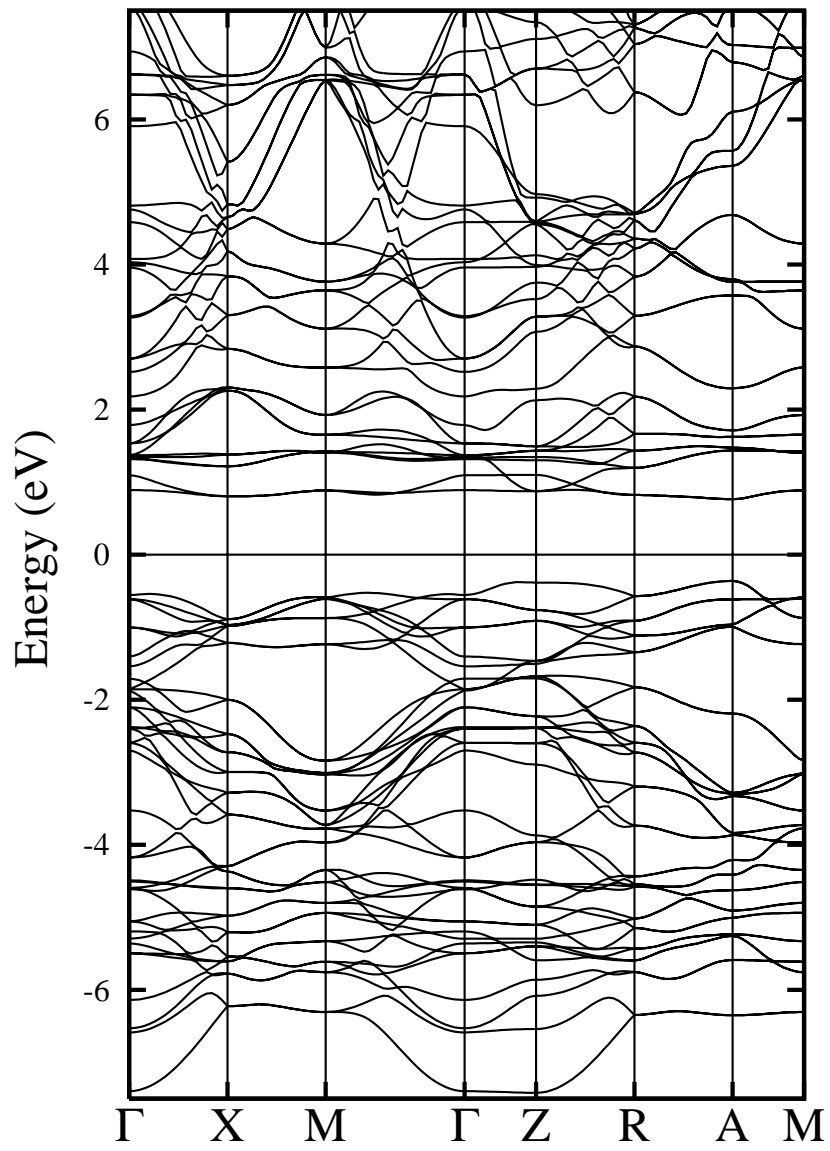
FIG. 7. Schematic diagram showing the checker-board-type charge order (CO), F-type orbital order (OO) and G-type ferrimagnetic spin order (SO) of Mn in  $\text{YBaMn}_2\text{O}_5$ .

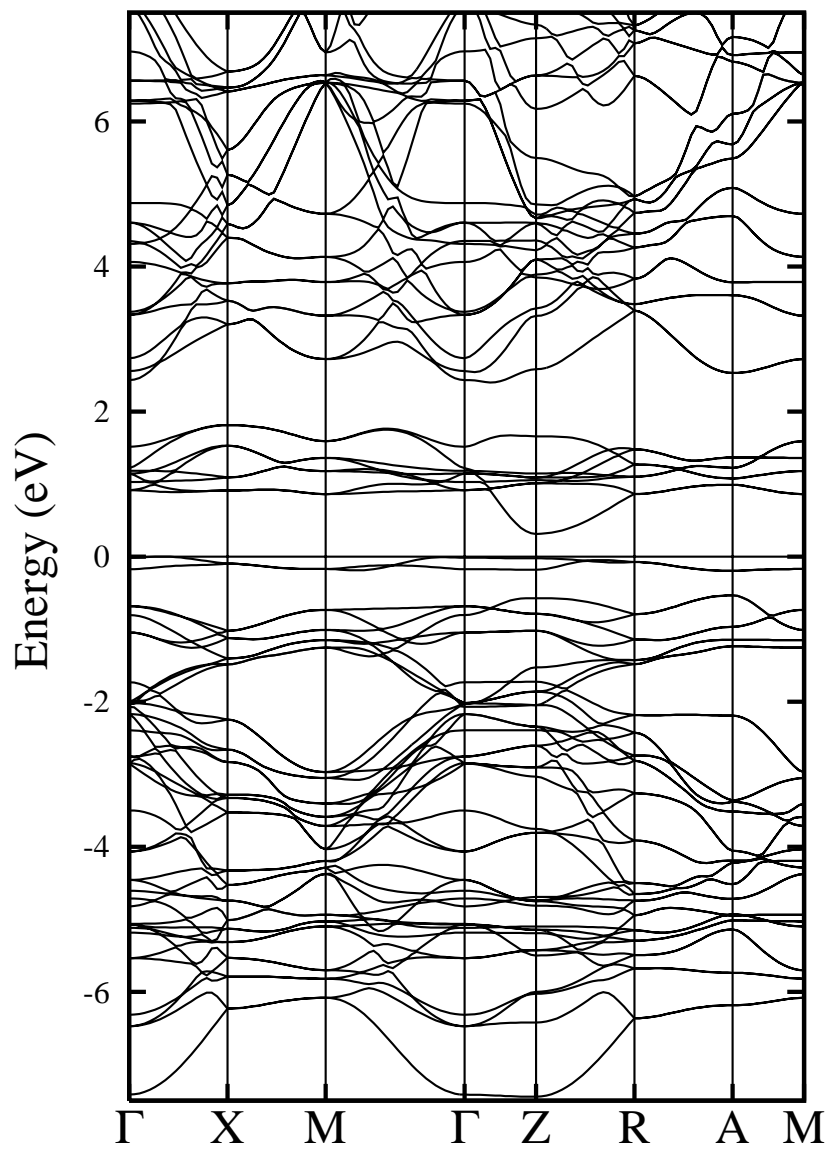
FIG. 8. Imaginary parts and real parts of the optical dielectric tensor of  $\text{YBaMn}_2\text{O}_5$  are given in the first and second panels, respectively (note that the spectra are broadened). The spin-projected imaginary parts of dielectric tensor along  $a$  and  $c$  directions are given in third and fourth panels, respectively.

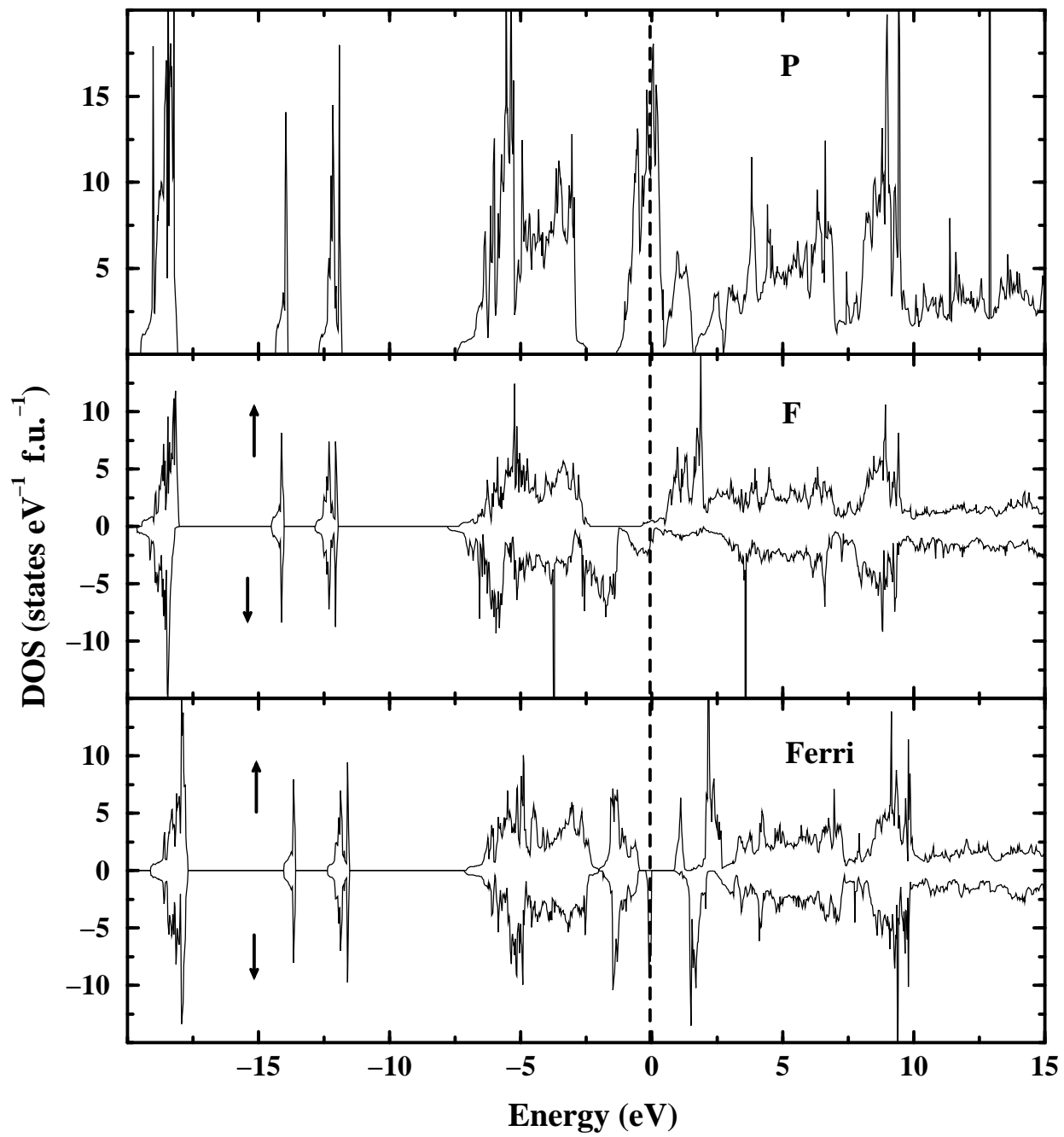
FIG. 9. Calculated reflectivity spectra, absorption coefficient [ $I(\omega)$  in  $10^5 \text{ cm}^{-1}$ ], and refractive index [ $n(\omega)$ ] along  $a$  and  $c$  for  $\text{YBaMn}_2\text{O}_5$ .

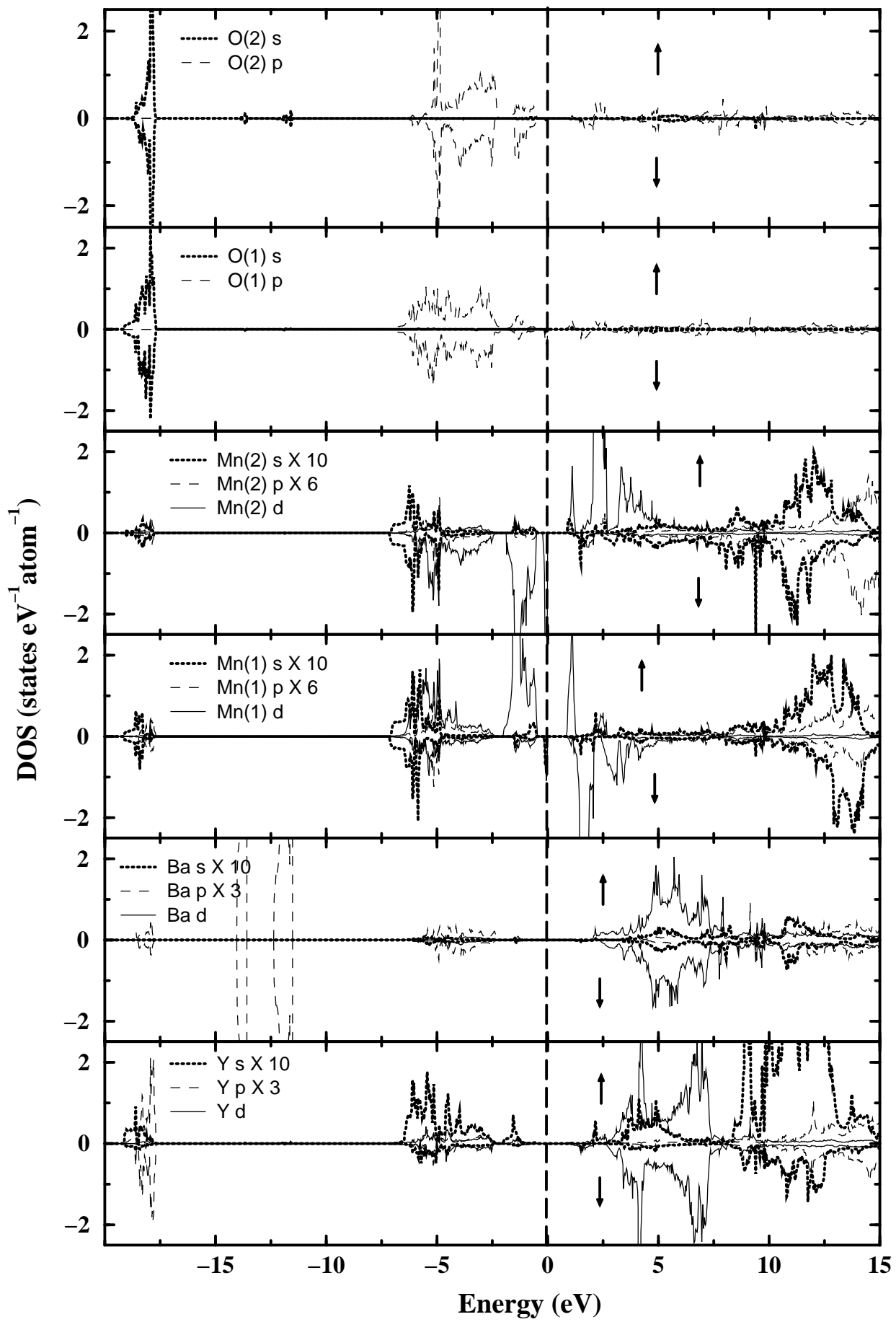
FIG. 10. Calculated  $K$ -edge spectra for Mn(1) and Mn(2) as well as O(1) and O(2) of  $\text{YBaMn}_2\text{O}_5$ .

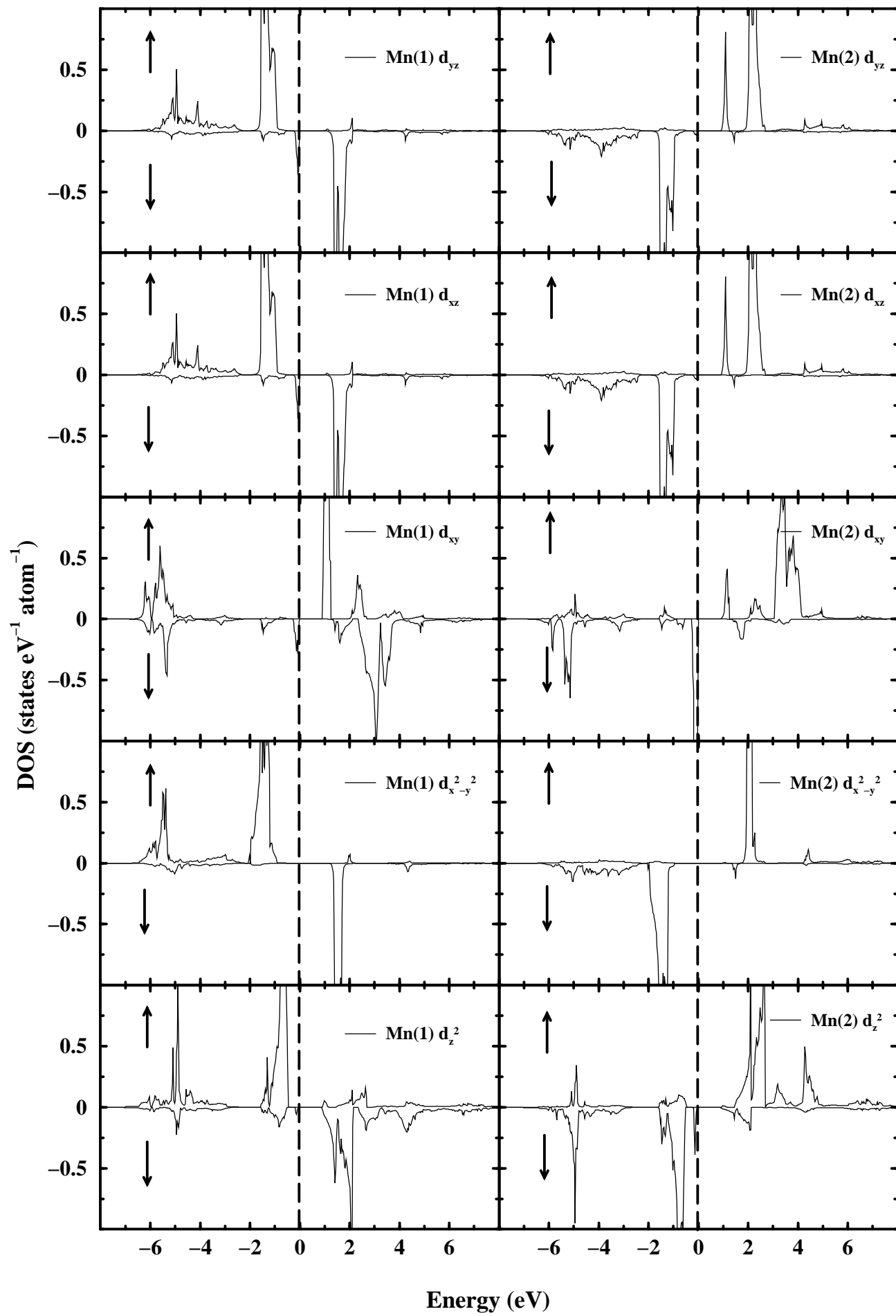


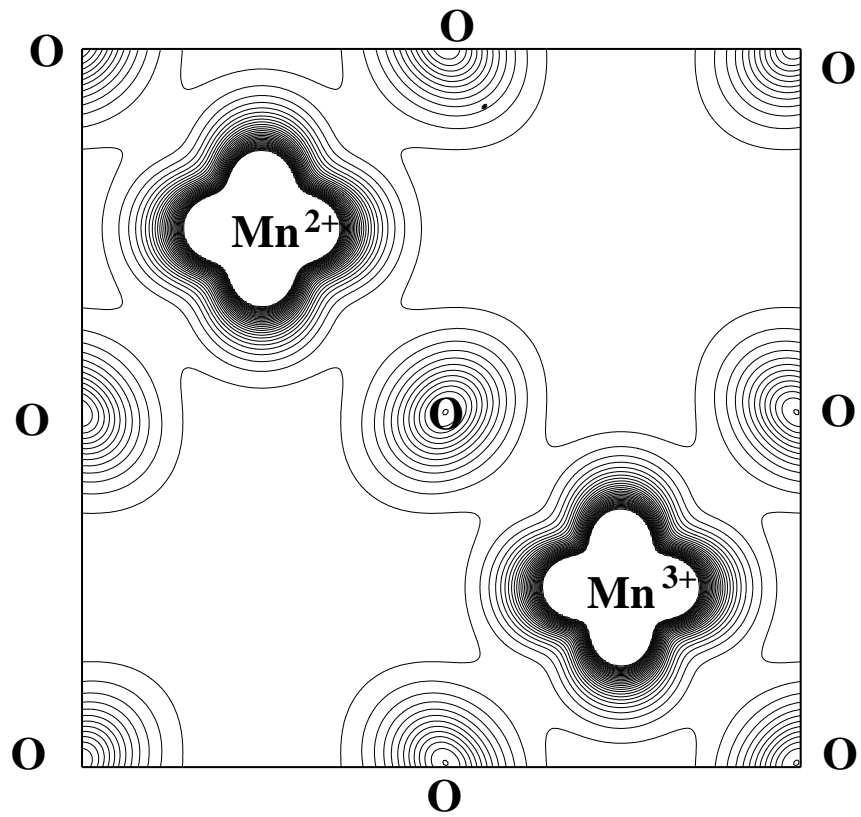




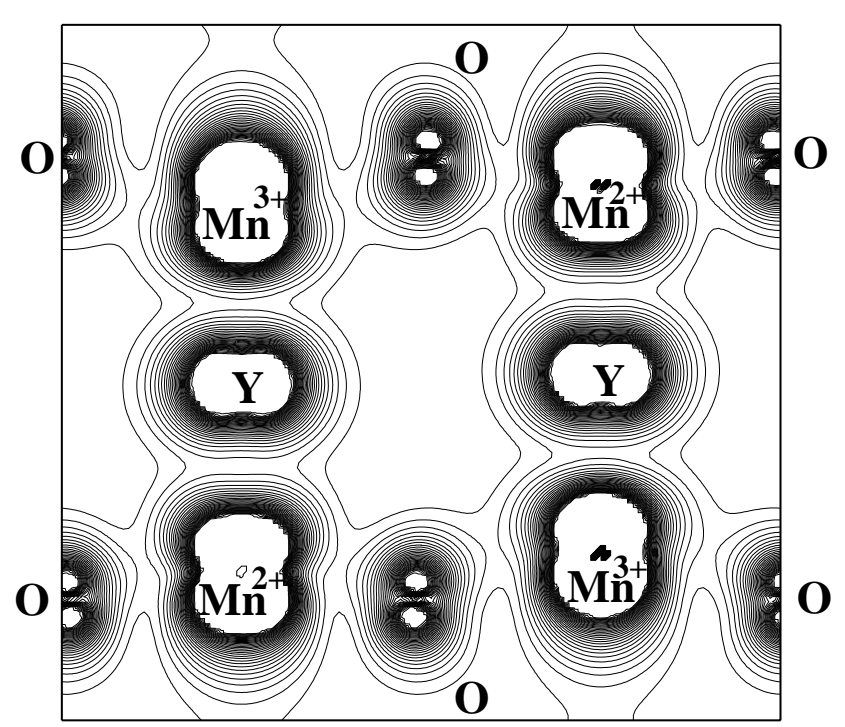




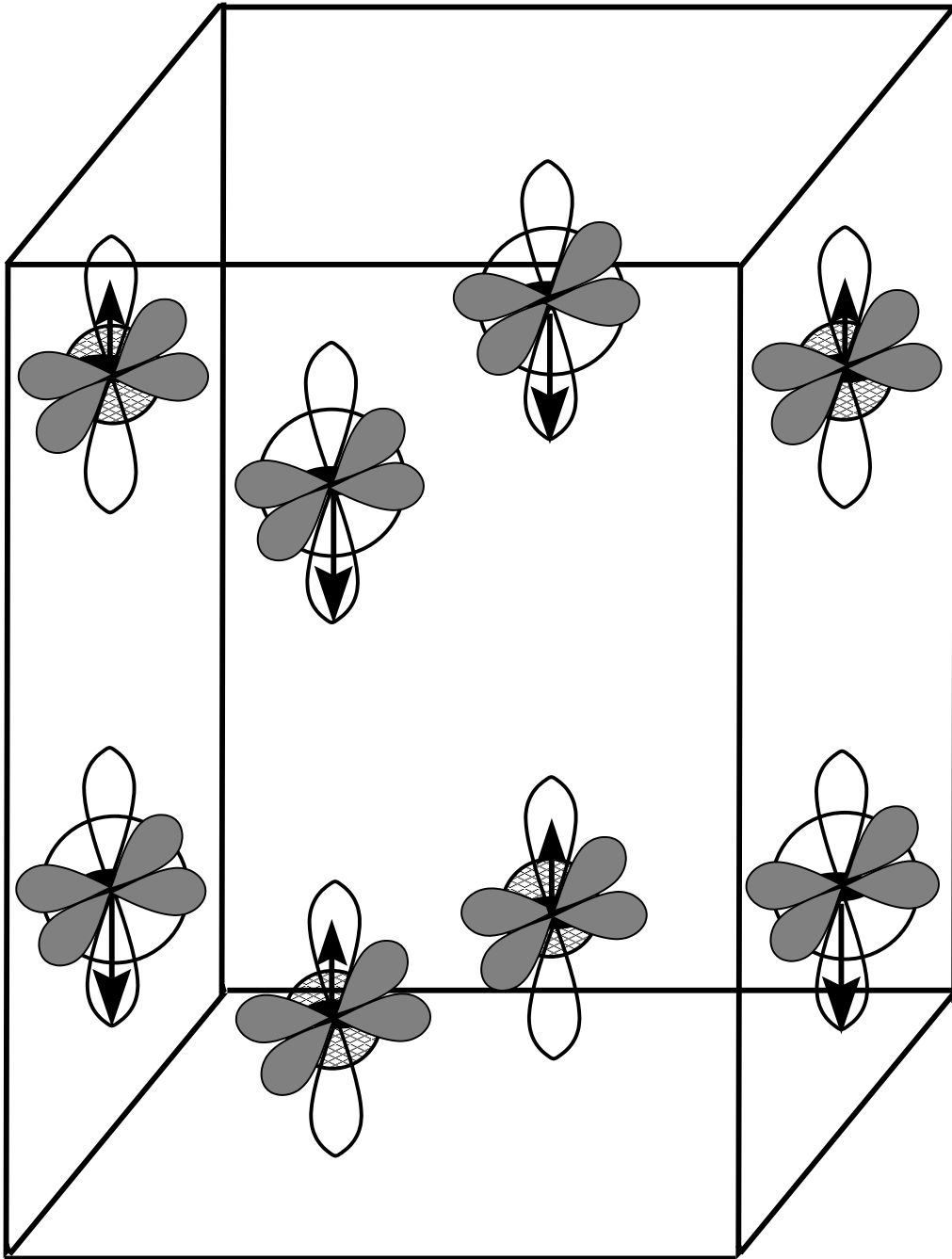


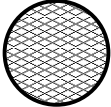
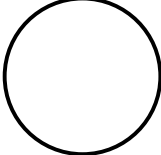


(a)



(b)



 **Mn<sup>3+</sup>**  
 **Mn<sup>2+</sup>**

